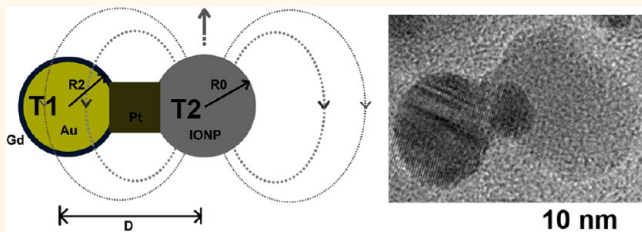


Hybrid Nanotrimers for Dual T_1 and T_2 -Weighted Magnetic Resonance Imaging

Kai Cheng,[†] Meng Yang,[†] Ruiping Zhang,^{†,‡} Chunxia Qin,[†] Xinhui Su,[†] and Zhen Cheng^{*,†}

[†]Molecular Imaging Program at Stanford (MIPS), Canary Center at Stanford for Cancer Early Detection, Department of Radiology and Bio-X Program, School of Medicine, Stanford University, 1201 Welch Road, Lucas P095, Stanford, California 94305-5484, United States and [‡]Department of Radiology, First Hospital of Shanxi Medical University, Taiyuan, Shanxi 030001, China

ABSTRACT Development of multifunctional nanoparticle-based probes for dual T_1 - and T_2 -weighted magnetic resonance imaging (MRI) could allow us to image and diagnose the tumors or other abnormalities in an exceptionally accurate and reliable manner. In this study, by fusing distinct nanocrystals *via* solid-state interfaces, we built hybrid heteronanostructures to combine both T_1 and T_2 -weighted contrast agents together for MRI with high accuracy and reliability. The resultant hybrid heterotrimers showed high stability in physiological conditions and could induce both simultaneous positive and negative contrast enhancements in MR images. Small animal positron emission tomography imaging study revealed that the hybrid heterostructures displayed favorable biodistribution and were suitable for *in vivo* imaging. Their potential as dual contrast agents for T_1 and T_2 -weighted MRI was further demonstrated by *in vitro* and *in vivo* imaging and relaxivity measurements.



KEYWORDS: hybrid · nanotrimers · dumbbell structures · T_1/T_2 -weighted magnetic resonance imaging · positron emission tomography

As one of the most powerful noninvasive diagnostic techniques, magnetic resonance imaging (MRI) is widely applied for clinical whole body imaging and can provide anatomical and functional information about soft tissues and organs with excellent spatial resolution. The signal intensity in MRI, corresponding to the magnetic relaxation rate of water protons, could be enhanced by appropriate exogenous contrast agents. There are two principal relaxation processes: longitudinal (T_1 recovery, spin–lattice) or transverse (T_2 decay, spin–spin) relaxation. T_1 recovery generates positive contrast, but T_2 decay reduces the imaging intensity, resulting in negative contrast.¹ The introduction of exogenous contrast agents could accelerate the relaxation process of either T_1 or T_2 , thereby enhancing the imaging contrast. Common T_1 contrast agents are paramagnetic complexes containing gadolinium (Gd^{3+}), manganese (Mn^{2+}), or iron (Fe^{3+}) ions.^{2–7} Those relatively small molecules usually have a short circulation time, due to their fast renal

excretion. They leave the vascular system within a few minutes, making it relatively hard to have a high resolution image acquisition. Moreover, the use of functionalized paramagnetic complexes as targeting contrast agents is limited because of the arduous and lengthy modification process and poor detection sensitivity. On the other hand, the superparamagnetic iron oxide nanoparticles (SPIOs) as T_2 MR contrast agents are very useful for biomedical applications as they are not subject to strong magnetic interactions in dispersion and are readily stabilized under physiological conditions.^{4,8} As T_2 -weighted contrast reagents, SPIOs can be magnetically saturated in the normal range of magnetic field strengths used in MRI scanners, thereby establishing a substantial locally perturbed dipolar field that leads to a remarkably shortening of proton relaxation of the surrounding solid tissue area.^{1,9} However, due to the negative contrast effect and susceptibility artifacts, distinguishing the region of signals induced by SPIOs from low-level background MR

* Address correspondence to zcheng@stanford.edu.

Received for review January 12, 2014 and accepted October 3, 2014.

Published online October 04, 2014
10.1021/nn500188y

© 2014 American Chemical Society

signals arising from adjacent tissues such as bone or vasculature is a major challenge, especially when the signal-to-noise ratio is low.

Recently, T_1/T_2 contrast agents have been developed and actively studied for dual T_1 and T_2 mode MRI, because they have the ability to validate reconstruction and visualization of the data in an accurate and reliable manner, and to acquire complementary and self-confirmed information to permit meaningful interpretation.¹⁰ Several approaches have been applied to develop T_1/T_2 contrast agents. In the first approach, some nanomaterials could intrinsically show both T_1 and T_2 contrast effects in the dual mode MRI but also suffer certain limitations. For instance, ultrasmall SPIOs (~ 3 nm size) display great potential as T_1 contrast agents, but their T_2 contrast effect is weak.¹¹ FeCo alloy nanoparticles (NPs) exhibit both high T_1 and T_2 contrast effects and the mechanism underlying this phenomenon is still unclear.¹² As paramagnetic materials, several lanthanide (Ln) oxide NPs (Ln = Gd, Dy, and Ho) and manganese oxide NPs have been extensively studied as potential candidates for either T_1 or T_2 MRI contrast agent or both.^{5,13–19} Compared to either regular T_1 or T_2 contrast agents, the MRI contrast effects of Ln oxide NPs are relatively weak at the same scanning condition. Moreover, their acute and chronic toxicity remain unclarified. In the second approach, in order to combine both T_1 and T_2 contrast effect together, Park and co-workers used Gd-labeled magnetite (Fe_3O_4) NPs as contrast agents for dual T_1 and T_2 weighted MRI.²⁰ Later, Cheon and co-workers found that the magnetic coupling induced by T_2/T_1 -core/shell structures can result in undesirable quenching of both T_1 and T_2 signals in MRI images.¹⁰ They then optimized the thickness of silica shell to modulate the degree of T_1 and T_2 coupling, thereby leading to a significant increase in T_1 contrast effect, but the T_2 contrast effect still lost one-third of original value because the thick silica shell dramatically reduces the magnetic field to the surrounding water molecules.¹⁰ On the basis of the similar IONP/silica core/shell structures, Yang and co-workers recently designed the dual-contrast T_1 and T_2 -weighted MR contrast agents modified with an arginine–glycine–aspartic acid (RGD) peptide for selectively targeting $\alpha_v\beta_3$ overexpressed tumor *in vitro* and *in vivo*.²¹ However, coupling of different chemical functionalities on a single component NP surface is often a strenuous and low yield synthetic process, and the presence of contrast agents and targeting molecules as well as other functional reporters on the same NP surface may interfere with the targeting capability and contrast effects. In the third approach, Gao and co-workers demonstrated that embedding Gd oxide crystals into iron oxide nanoparticles could synergistically enhance both T_1 and T_2 contrast effects in MR imaging, probably due to the fact that the Gd spins of Gd_2O_3 buried in iron oxide NPs are parallel to the local magnetic field induced by those

superparamagnetic iron oxide NPs under an external magnetic field.²² This strategy is attractive for some reasons such as facile and reproducible synthetic methods, though challenges still remain if ones try to incorporate targeting moieties and biocompatible coating on the single external surface of those NPs.

The interference inevitably occurs when both T_1 and T_2 contrast agents are integrated into a single composite, especially when they are in close proximity. Although the conventional core/shell structures could efficiently reduce their magnetic coupling by introducing a separating layer between them (Figure 1a, left panel), the T_2 contrast effect is compromised as the thick shell decreases the magnetic field to the surrounding water molecules. In this study, we first developed a synthetic strategy for engineering the architecture of heterogeneous nanoparticles, which could help us to further understand the magnetic coupling at the nanoscale. After gaining insight from the synthesis strategies, we chose dumbbell-like NPs or so-called 'Janus' NPs, which have two different components within one single structure, as solid-state analogues of bifunctional organic molecules to construct hybrid nanotrimers (HNTs) (Figure 1a, the right panel), in which iron oxide and gold nanocrystals are connected with a platinum nanocube. In our previous study, dumbbell-like heteronanostructures with two different nanomaterials (Au and iron oxide: Au–IO) within one hybrid structure also showed capability of combining two different moieties together for dual modal imaging.²³ In this study, the surface of Au component in Au–IO NPs were then modified with Gd to test its use for T_1/T_2 MRI. However, induced T_1 contrast effect could be adversely affected by the attenuation of local magnetic field because there is a strong magnetic coupling between iron oxide and Gd species in the structure of the dumbbell-like Au–IO NPs. To reduce the undesired magnetic coupling effect, we designed a strategy to build such HNTs to combine both T_1 and T_2 contrast agents together by fusing IONP, Pt, and gold nanocrystals *via* solid-state interfaces (Figure 1b). The size of gold nanocrystals could be further enlarged by controlling the seed-mediated and epitaxial growth processes during the synthesis. Meanwhile, we optimized the sizes of Pt cubes to adjust the distance of IONP and gold nanocrystals in order to manipulate the magnetic coupling effect. The resultant heterotrimers with large gold crystals show real dumbbell morphology, which are named as dumbbell-hybrid nanotrimers (DB-HNTs). Ones with a large center-to-center distance between gold and iron oxide are called as extra large dumbbell-hybrid nanotrimers (XDB-HNTs). The iron oxide components were modified with polyethylene glycol (PEG) chains to make the whole NPs water-soluble and biocompatible. The surface of gold were covalently immobilized with Gd chelators (dithiol derivative 1,4,7,10-tetraazacyclododecane-1,4,7,10-tetraacetic acid

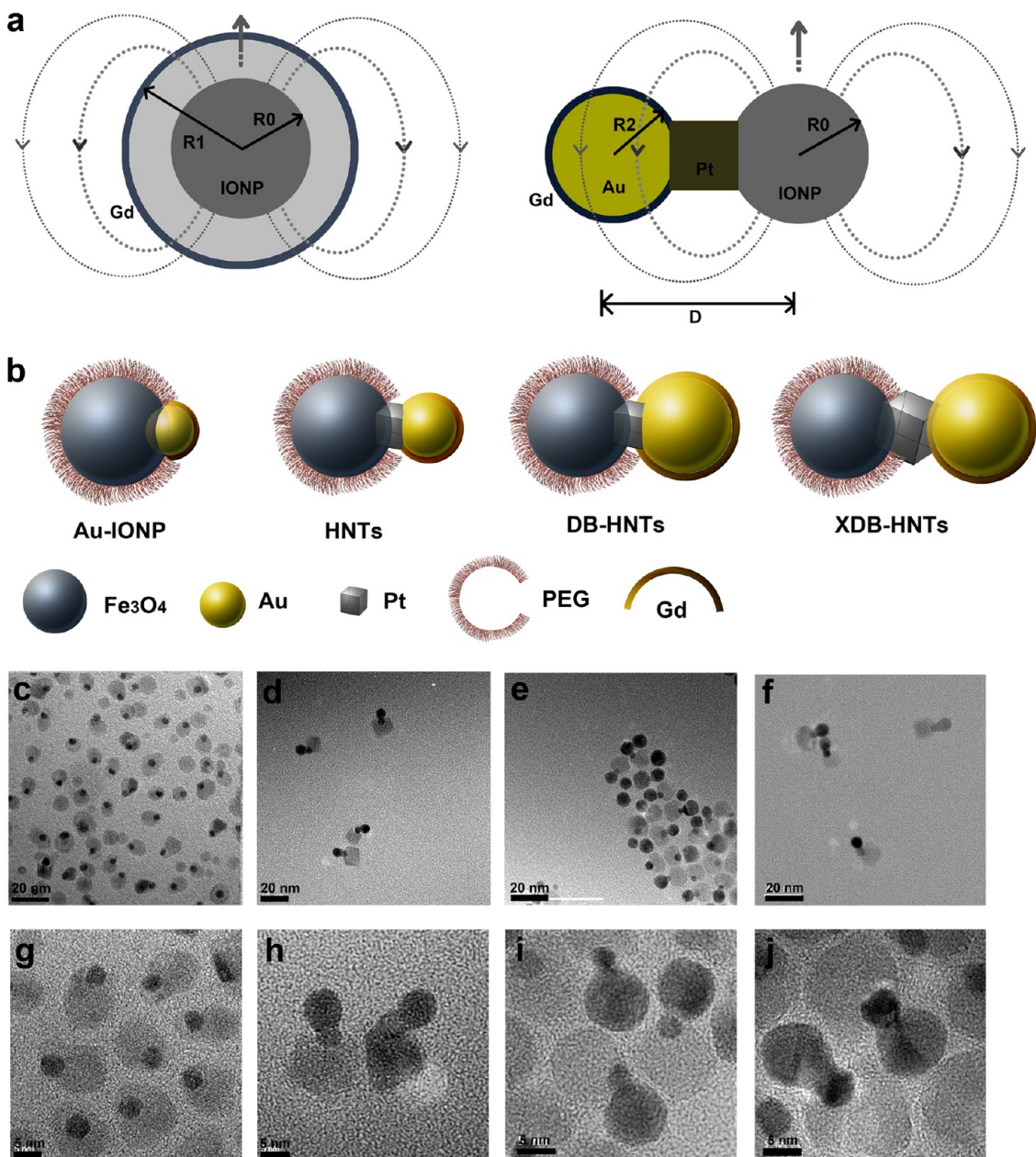


Figure 1. (a) Engineering the heterogeneous nanostructures for magnetic coupling of T_1 and T_2 contrast agents with (left) core/shell structures or (right) dumbbell structures. R_0 is the radius of T_2 contrast agent (iron oxide nanoparticles), R_1 is the radius of Gd shell, R_2 is the radius of gold nanoparticles, and D represents the center-to-center distance between iron oxide and gold nanoparticles. (b) Design and characterization of dumbbell heterostructures for dual T_1 and T_2 -weighted magnetic resonance imaging. Illustration of constructions of four different types of dumbbell-like or dumbbell heterostructures (Au-IONPs, HNTs, DB-HNTs, and extra-large DB-HNTs (XDB-HNTs)). (c–f) TEM images of four types of heterostructures. (g–j) High-resolution TEM (HR-TEM) of four types of heterostructures.

(DOTA) chelator, or cystamine-DOTA₂, Supporting Information Figure S1). The resultant hybrid heterostructures could induce both simultaneous positive and negative contrast enhancement in MR images. The *in vivo* biodistribution of hybrid heterostructures favorable for molecular imaging was confirmed using small animal PET. The potential of Gd-DB-HNTs as dual contrast agents for T_1 and T_2 -weighted MRI was demonstrated by conducting *in vitro* relaxivity measurements and *in vivo* imaging.

RESULTS AND DISCUSSION

Synthesis and Characterization of Dumbbell Hybrid Heterostructures. The syntheses of complex hybrid heteronanostructures sequentially involved a set of the seed-mediated nucleation and epitaxial growth processes. According to the previously published procedures with a slight modification,^{23–25} the monodisperse Au-IONP heterodimers were synthesized by thermal decomposition of iron precursor

TABLE 1. Summary of Size Measurement by TEM and DLS and Zeta Potentials of Various Heteronanoparticles

sample	TEM analysis (nm) ^a			$D_{\text{Au-to-IO}}$ (nm) ^b	DLS (nm)	zeta potential (mV)
	IONP	Pt	Au			
Au-IONP	10.2 \pm 0.6	-	5.1 \pm 0.4	5.4 \pm 0.5	19.5 \pm 0.6	-13.4 \pm 0.8
HNTs	11.6 \pm 0.6	4.3 \pm 0.2	7.0 \pm 0.4	9.6 \pm 0.6	21.2 \pm 0.5	-15.1 \pm 0.9
DB-HNTs	11.7 \pm 0.4	4.3 \pm 0.3	9.1 \pm 0.6	10.7 \pm 0.7	24.6 \pm 0.7	-16.0 \pm 1.3
XDB-HNTs	12.5 \pm 1.2	5.1 \pm 0.5	9.8 \pm 0.6	12.9 \pm 0.7	26.8 \pm 0.9	-16.4 \pm 1.2

^a A minimum of 200 discrete particles was measured from each of at least two widely separated regions of the sample. ^b D : the center-to-center distance between iron oxide and gold nanocrystal.

(iron pentacarbonyl) onto 5 nm polyhedral gold nanospheres in the presence of surfactants (oleic acid and oleylamine), followed by a controlled oxidation. When cubic Pt nanoparticles (4 nm Pt NPs) were used as seeds, the site-selective heterogeneous nucleation and epitaxial growth resulted in the formation of Pt-IONP heterodimers,^{26,27} which showed uniform heterodimer morphology with a narrow size distribution (Supporting Information Figure S2). The Pt and IONP components within Pt-IONP heterodimers have average sizes of 4.3 ± 0.2 and 11.6 ± 0.6 nm, respectively (Table 1, Supporting Information Figure S3). As solid-state analogues of functional organic molecules, such Pt-IONP hybrid heterodimers have different chemical and physical interfaces and could further behave as cross-linkers to combine different nanocomponents together to construct more complex heterostructures in a stepwise and predictable manner.^{27,28} Here, by using Pt-IONPs as building blocks, we have successfully prepared HNTs with size-tunable Au components (Figure 1d–f). Typically, in the presence of Pt-IONP heterodimers as seeds, the reduction of gold precursor [hydrogen tetrachloroaurate(III) (HAuCl₄)] with oleylamine in a mild temperature results in the heterogeneous nucleation of Au on the Pt components. Such selective overgrowth of gold on the Pt-IONP seeds is attributed to both the lattice matching between Pt and Au components, and the stress energy accumulated at the heterogeneous interface between gold and iron oxide.^{28,29} The HNTs were observed as heterotrimer morphology in approximately 85% yield (a minimum of 200 discrete particles were measured from each of at least two widely separated regions of the sample) in the transmission electron microscopy (TEM) images (Figure 1d). The average diameter of spherical Au components of HNTs is approximately 7.0 ± 0.4 nm. To increase the size of Au components, an extra amount of gold precursor is added during the synthesis under a similar condition. As seen in Figure 1e,i, Au components of the resultant dumbbell HNTs (DB-HNTs) have average diameters of 9.1 ± 0.6 nm (Table 1). To manipulate the magnetic coupling effect, we optimized the sizes of cubic Pt nanocrystals to adjust the distance of iron oxide components and gold nanocrystals. When 5 nm Pt

nanocubes were used as seeds (Supporting Information Figure S2), we could end up with getting extra large dumbbell HNTs (XDB-HNTs) (Figure 1f,j). As shown in Table 1, the center-to-center distance between iron oxide and gold nanocrystal ($D_{\text{Au-to-IO}}$) was significantly increased when large gold nanocrystals were grown on the Pt seeds. As expected, the large 5 nm Pt nanocubes created the longest distance (12.9 ± 0.7 nm) between iron oxide and gold within XDB-HNTs. Although much bigger HNTs with similar dumbbell shapes could be obtained when the 7 nm cubic Pt particles were used as seeds, two or more gold crystals could grow on Pt cubes to form complex heterostructures (Supporting Information Figure S6), which could adversely influence the quality of the products. In short, all four heterostructures (Au-IONP, HNTs, DB-HNTs, and XDB-HNTs) share a structural similarity, a dumbbell shape, in which either Au component is embedded into IONP, or Au and IONP are connected via a robust Pt spacer.

High-resolution TEM (HRTEM) images of HNTs indicate that all three components are well-crystallized and they have coherent interfaces (Figure 2). The d -spacing between adjacent (111) planes in IONP component is 4.84 Å, which is characteristic of magnetite. The lattice fringes of Pt and Au components are very similar (2.20 and 2.32 Å, respectively) and they are related to (111) planes of Pt or Au in the fcc phase. Moreover, the d -spacing of Pt is approximately half of that of the (111) planes of Fe₃O₄. Thus, the formation and stability of Pt-IONP and Pt-Au interfaces are largely attributed to their lattice matching. Energy-dispersive X-ray spectroscopy (EDS) was further applied to determine the compositions of various HNT nanostructures (Figure 2b and Supporting Information Figures S4 and S5). It is apparent that the HNTs are composed of Fe₃O₄, Pt and Au crystals. The forward and inverse Fast Fourier transforms (FFT) were applied to corresponding HR-TEM images to distinguish iron oxide, cubic Pt, and Au nanocrystals within various HNTs. The inset in diffractogram pattern (Figure 2c) of HNTs showed the splits of the (111) peaks into two spots: one for Pt and the other for Au crystal, due to the slight difference in planar distances of the Pt and Au crystals. Inverse FFT reconstructions of IO, Pt, or Au NPs

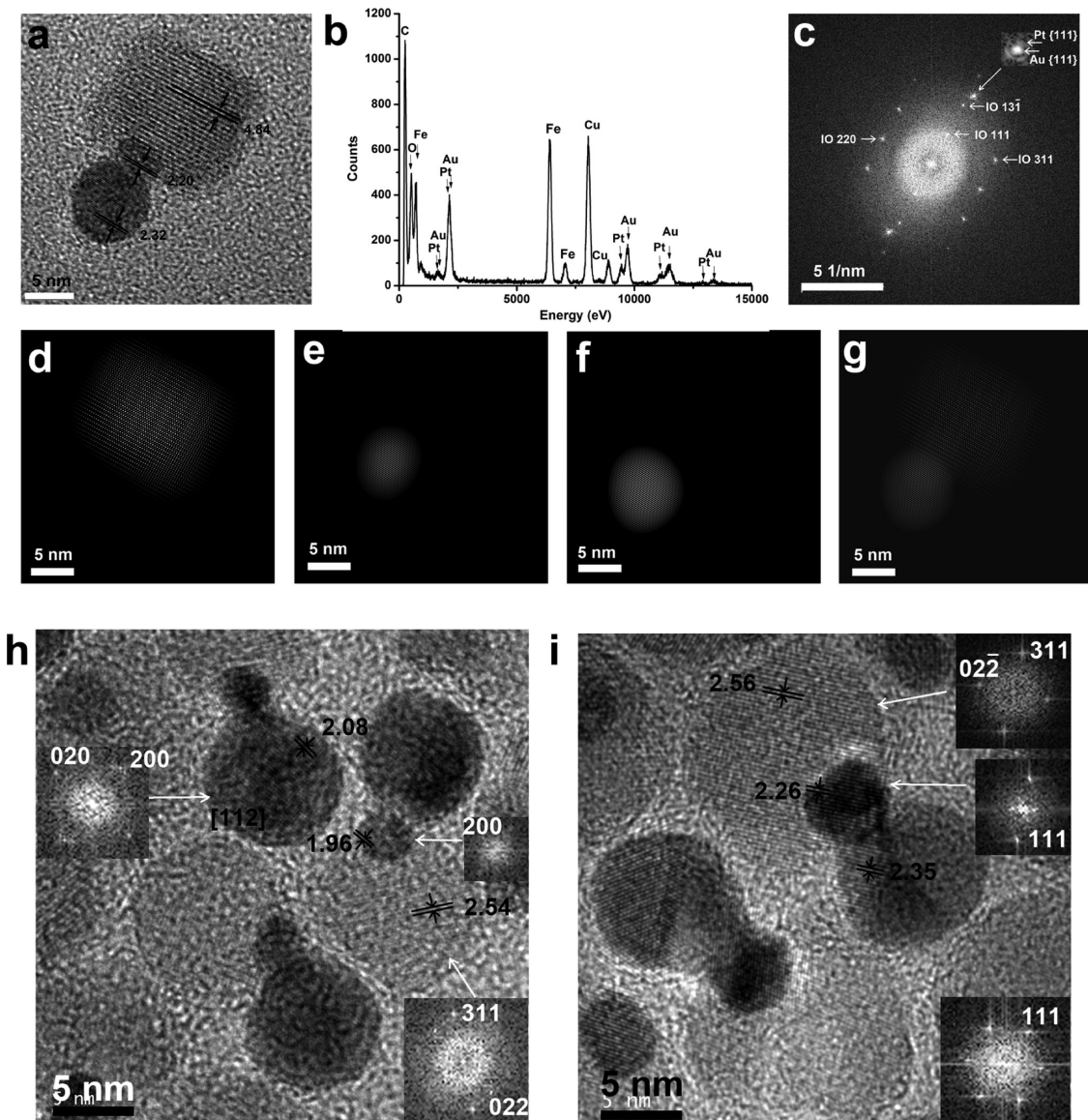


Figure 2. TEM characterization of three types of HNTs. (a) HR-TEM of HNTs; (b) energy-dispersive X-ray spectroscopy (EDS) spectrum of HNTs. The copper and carbon signals came from the TEM grid. (c) The Fourier transform of image recorded from (a). (d–f) Corresponding inverse-Fourier-transform of each component. (g) Overlay image of reconstructed each component. (h) HR-TEM analysis of DB-HNTs. The Fourier filtered images recorded from each component were shown on the insets. (i) HR-TEM analysis of XDB-HNTs. The Fourier filtered images recorded from each component were shown on the insets. Lengths of d are in Å.

using their own reflections provided the real-spatial distributions of IO, Pt, and Au in HNTs (Figure 2d–f). It was further confirmed by the overlay image of all reconstructed IO, Pt and Au inverse FFT images (Figure 2g). Likewise, the lattice images of DB-HNTs and XDB-HNTs coupled with the forward FFT images revealed the crystal structures and orientations of Au and IONP around Pt cube (Figure 2h,i). All of components showed well-defined crystal structures and coherent interfaces. Importantly, they all have dumbbell shapes; Au and IONP component are tightly connected to each other via a cubic Pt crystal.

As seen in Supporting Information Figure S7, all of dumbbell HNTs are superparamagnetic at room

temperature and they all show similar loops with saturation moment of 26 emu/g of Fe_3O_4 . The slow increase in magnetic moment from hysteresis loops with the field up to 5T is due to the interface communication between the nanoscale Pt, Au, and Fe_3O_4 crystals, which leads to the change of magnetization behaviors of Fe_3O_4 nanoparticles within all types of HNTs.²⁴

Surface Coating and Gd Chelating of Hybrid Heteronanostructures. A surface modification step is necessary to provide the NPs water-soluble, biocompatible and functionalizable. According to our previously published procedure,²³ all four hybrid heterostructures were coated with biocompatible PEG chains in order

TABLE 2. Elemental Analysis of Various Dumbbell Heterostructures

heterostructures	weight ratio (Fe/Pt/Au/Gd)	mole ratio (Fe/Pt/Au/Gd)	component ratio ^a (IONP/Pt/Au)	Gd per NP
Gd–Au–IONPs	1:0.45:0.047	1:0.13:0.017	1:0.96	391 ± 23
Gd–HNTs	1:0.47:1.21:0.10	1:0.13:0.34:0.037	1:0.87:1.10	1139 ± 53
Gd–DB–HNTs	1:0.50:2.71:0.23	1:0.14:0.77:0.083	1:0.92:1.09	2438 ± 39
Gd–XDB–HNTs	1:0.68:2.74:0.22	1:0.19:0.78:0.079	1:0.89:1.11	2925 ± 46

^a The size of each individual component was measured by HRTEM. Each type of heterostructure displays well-controlled morphology and chemical composition so that each particle concentration could be calculated based on its own geometrical parameters and elemental composition.

to circumvent the known scavenging effects of the mononuclear phagocyte system (MPS) and to prolong their blood circulation half-life. Such PEGylation process refers to the approach of the ligand exchange in which the bidentate ligand (dopamine) terminated PEG (MW ~ 5000 Da, Supporting Information Figure S8) chains were covalently attached onto the surface of IONP components. It enables the phase transfer of the NPs from organic solvents to an aqueous solution, and renders the NPs with great stability against agglomeration in physiological conditions. More importantly, it provides functional groups or moieties for potential targeting modification.

Because of significant differences in the surface chemistry properties between Au and iron oxide components, the Au surface could be selectively modified by well-defined functional groups without any interference from the other components of heterostructures. Here, a dithiol derivative DOTA chelate (cystamine–DOTA₂, Supporting Information Figure S1) was synthesized and immobilized on the Au surfaces *via* a strong gold–sulfur interaction. Combining two DOTA molecules *via* a dithiol linker could guarantee the maximum coverage of DOTA chelates on the gold surface (Table 1). The DOTA modified heterostructures were then conjugated with Gd³⁺ by mixing solution of NPs with a large excess of aqueous solution of GdCl₃. After purification, the amount of each element in the resultant Gd-incorporated NPs was determined by inductively coupled plasma–mass spectroscopy (ICP–MS). As listed in the Table 2, the weight and molar ratios of Fe/Pt/Au/Gd of four types of heterostructures were calculated according to the ICP–MS analytical results. As described previously, each type of heterostructure displays well-controlled morphology and chemical composition so that each particle concentration could be calculated based on its own geometrical parameters and elemental composition. The number of Gd per single Gd–DB–HNT is 2438 ± 39 (mean ± SD), more than twice as much as that of Gd–HNT (1139 ± 53), largely because the former has much larger gold component than the latter. As expected, Gd–XDB–HNTs with larger gold component have more Gd molecules (2925 ± 46) than Gd–DB–HNTs. Since part of gold surface is embedded into the iron oxide component, Au–IONPs have much less Gd molecules (391 ± 23) compared to the others. It is noticed that

by increasing the size of spherical gold component, both Gd–DB–HNTs and Gd–XDB–HNTs have much higher Gd/Fe molar ratios (0.083 or 0.079) than Gd–HNTs (0.037).

The hydrodynamic sizes and zeta potentials of four types of heterostructures were determined by dynamic light scattering (DLS) analysis. The average hydrodynamic diameters of Au–IONPs, HNTs, DB–HNTs, and XDB–HNTs were 19.5 ± 0.6, 21.2 ± 0.5, 24.6 ± 0.7, and 26.8 ± 0.9 nm, respectively (Table 1 and Supporting Information Figure S10). A significant increase in size from 19 to 27 nm was attributed to the epitaxial growth of gold components on Pt crystals. After the gold components were coated with negatively charged DOTA ligand, zeta potential measurements clearly showed that all four types of heterostructures had negative surface potentials (Table 1). Subsequent complexation with Gd ions gave rise to a remarkable increase in surface zeta potentials of all four NPs (Supporting Information Figure S12), due to the neutralization of the negative surface charge caused by the coordination of cationic Gd ions with carboxylate groups of DOTA ligands.

Magnetic Resonance (MR) Phantom Test. To evaluate the feasibility of using various Gd incorporated HNTs as dual *T*₁- and *T*₂-weighted contrast agents, we measured their relaxivities in aqueous medium on a 7.0 T MR scanner. Figure 3 shows the *T*₁-weighted MR images of Gd–Au–IONPs, Gd–HNTs, Gd–DB–HNTs, and Gd–XDB–HNTs at different concentrations based on iron contents. Both Gd–DB–HNTs and Gd–XDB–HNTs displayed a signal enhancement on the *T*₁-weighted images with a concentration-dependent manner. It is noticed that their contrast effects are more significant than that of Gd–HNTs at the same condition, but there is almost no *T*₁ contrast effect observed for Gd–Au–IONPs. Although the larger Au surface area could result in the more Gd loading, the distance between Au and IONP components played an important role in regulating the magnetic coupling effect so that both Gd–DB–HNTs and Gd–XDB–HNTs provided the most significant contrast effect among these heterostructures. To quantitatively determine the MR contrast effect, the relaxivity coefficient (*r*₁) was calculated from *T*₁ mapping images acquired by using an inversion recovery sequence. On the basis of the total concentrations of both Fe and Gd, the *r*₁

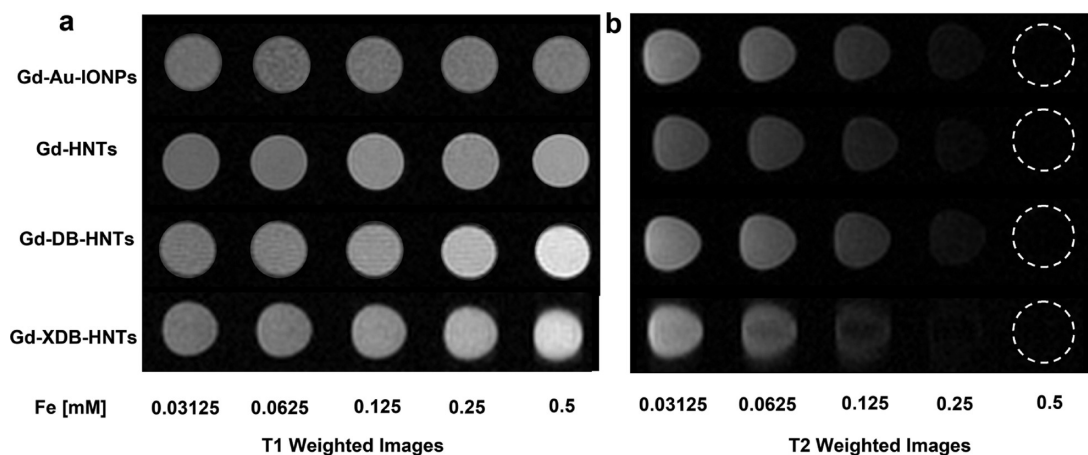


Figure 3. (a) T_1 - and (b) T_2 -weighted MR images of dumbbell hybrid heterostructures (Gd-Au-IONPs, Gd-HNTs, Gd-DB-HNTs, and Gd-XDB-HNTs).

TABLE 3. r_1 and r_2 of Various Dumbbell Heterostructures and DOTarem

heterostructures	r_1 (mM $[Fe + Gd]^{-1}/s$)	r_1' (mM $[Gd]^{-1}/s$)	r_2 (mM $[Fe]^{-1}/s$)	r_2/r_1	r_2/r_1'
Gd-Au-IONPs	1.65	43.6	123	2.8	75
Gd-HNTs	1.74	18.6	131	7.0	75
Gd-DB-HNTs	3.88	30.4	128	4.2	33
DB-HNTs	2.34	-	125	-	-
Gd-XDB-HNTs	4.13	32.1	136	4.2	33
DOTarem	-	2.75	2.02	0.73	-

values of Gd-Au-IONPs, Gd-HNTs, Gd-DB-HNTs, and Gd-XDB-HNTs are 1.65, 1.74, 3.88, and 4.12 mM⁻¹/s, respectively (Table 3). It is clear that Gd-DB-HNTs have 141% higher r_1 value compared to the commercial contrast agent, DOTarem (godoxate meglumine, Guerbet, Aulnaysous-Bois, France, $r_1 = 2.75$ mM⁻¹/s), due largely to the slower tumbling rate of Gd-complex on the NPs than as free molecules.² For Gd-HNTs, however, the T_1 MR contrast effect was quenched to some extent because the coupling between electron spins of the Gd complex and nuclear spins of water was perturbed by the additional magnetic field generated by nearby iron oxide components.¹⁰ Such quenching effect could be remarkably reduced by enlarging the distance between T_1 and T_2 contrast agents (or $D_{Au\text{-to-}IO}$). In this case, with an increase in the size of gold components, the percentage of Gd-complex immobilized on gold surface away from the iron oxide components gradually increased, thereby resulting in reduction of the quenching effect. In a similar manner, the interaction between the T_1 and T_2 contrast agents could be efficiently separated or attenuated using large Pt nanocubes. With the larger center-to-center distance between iron oxide and gold component, Gd-XDB-HNTs provided higher r_1 value than Gd-DB-HNTs. Both Gd-DB-HNTs and Gd-XDB-HNTs showed obvious T_1 contrast effect among four heterostructures. On the other hand, the iron oxide components in the heterostructures can serve as T_2 contrast enhancement agents. Since all

four heterostructures have iron oxide components with similar sizes and shapes, their T_2 weighted MR images at a same iron concentration gradient (in the range from 0 to 0.5 mM) displayed similar contrast effects (Figure 4b). Accordingly, the relaxivity coefficients (r_2) of Gd-Au-IONPs, Gd-HNTs, Gd-DB-HNTs, and Gd-XDB-HNTs were calculated from T_2 mapping images (Table 3). Because the sizes of iron oxide components are roughly close, they all have similar relaxivities, which are close to that of a commercial available T_2 contrast agent (Feridex, 158.3 mM⁻¹/s). It suggests that all heterostructures with iron oxides can be efficiently used as T_2 contrast agents. Moreover, there are no significant changes in relaxivity of Gd-chelated NPs compared to that of unchelated NPs, indicating that the T_2 relaxation process induced by magnetic iron oxide cores could not be adversely influenced by the Gd-coating on the nearby Au components. Interestingly, there is a slight decrease in relaxivity coefficient with a decrease in the size of iron oxide component (Tables 1 and 3), probably due to both thermal agitation and the surface spin canting of small iron oxide particles. Finally, the ratios of r_2 to r_1 are calculated in order to estimate the efficiency of both T_1 and T_2 contrast effects of all the heterostructures. For the purpose of comparison, we determined each relaxivity of contrast agent with each element content. For example, the calculation of the r_1 relaxivity of each particle is based on different concentrations of Gd. They are listed as r_1' values in

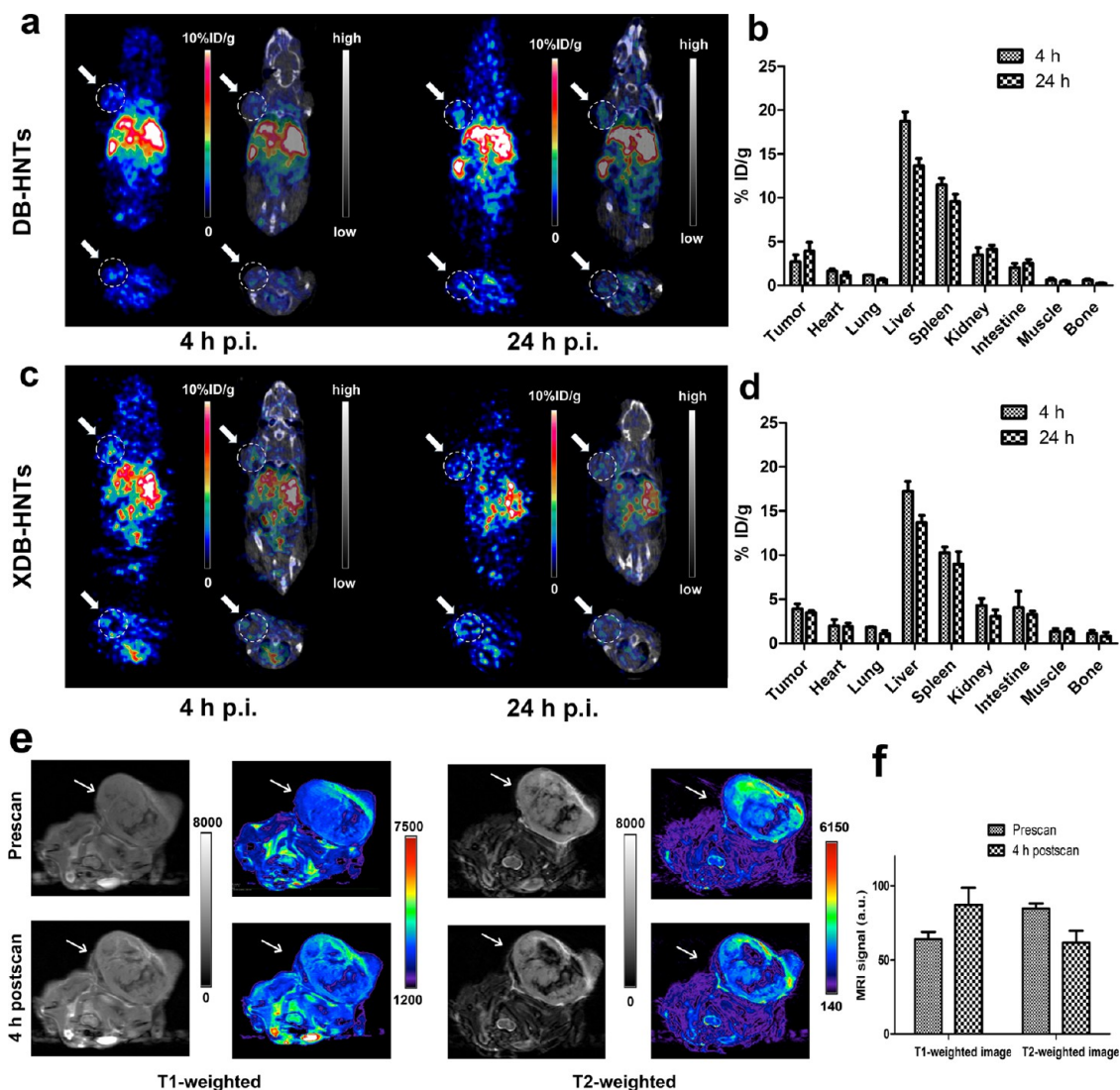


Figure 4. (a) *In vivo* small animal PET/CT images (left, PET image alone; right, PET/CT merged image) of HT-29 tumor bearing mice ($n = 3$) after 4 and 24 h postinjections of ^{64}Cu -DB-HNTs. (b) PET image quantification analysis of the ^{64}Cu -DB-HNTs in major organs and tissues. (c) *In vivo* small animal PET/CT images (left, PET image alone; right, PET/CT merged image) of HT-29 tumor bearing mice after 4 and 24 h postinjections of ^{64}Cu -XDB-HNTs. (d) PET image quantification analysis of the ^{64}Cu -XDB-HNTs in major organs and tissues. (e) T_1 - and T_2 -weighted magnetic resonance images of HT-29 tumor bearing mice ($n = 3$) before and after intravenous injection of Gd-DB-HNTs. The left ones show gray scale images, and the right ones show the pseudocolored images (NIH look-up tables (LUTs)). (f) MRI quantification analysis of tumors uptake of Gd-DB-HNTs at pre- and postscan. The left ones show gray scale images, and the right ones show the pseudocolored images (NIH LUTs). White arrows indicate the tumors.

Table 3. Even though the r_2/r_1 ratio of Gd-DB-HNTs was 33, their r_2/r_1' ratio was only 4.2, indicating that they could be both efficient T_1 and T_2 contrast agents. Although Gd-XDB-HNTs have slightly higher r_1' values, they do not have better r_2/r_1 ratio than Gd-DB-HNTs because of their larger size of iron oxide component.

Stability and Cytotoxicity. To validate the stability of functionalized heterostructures, we measured the hydrodynamic size distribution of functionalized DB-HNTs over the time course of a 48 h incubation in mouse serum using DLS. The average sizes of DB-HNTs remained same over the course of 48 h incubation, indicating that the DB-HNTs are stable

in a physiological condition (Supporting Information Figure S11a). We further validated the binding stability of Gd ions to the functionalized DB-HNTs by analyzing the trace amount of each element in the eluent/supernatant of every aliquot from stability test ICP-MS, and found the free Gd^{3+} was nearly undetectable (Supporting Information Figure S13). The absence of any free Gd ions in the eluent confirmed the strong binding of Gd ions to DOTA-conjugated DB-HNTs.

In vitro cytotoxicity of Gd-DB-HNTs was evaluated by a standard tetrazolium dye (MTT) based colorimetric assay of viability of a fibroblast cell line (NIH-3T3). As seen in Supporting Information Figure S11b, there was no obvious decrease in cell viability after the cells were

incubated with Gd–DB-HNTs at various concentrations in the range of 1–200 μg Fe/mL for 24 and 48 h. The cell viability still remained above 90% for 24 h or 85% for 48 h even at the concentration of 200 μg Fe/mL, indicating that Gd–DB-HNTs are biocompatible and minimally cytotoxic in the given concentration range.

PET Imaging and Quantification. The *in vivo* behavior of DB-HNTs was then evaluated by positron emission tomography (PET). Instead of being chelated with Gd ions for MRI study, the DOTA molecules on the DB-HNTs were efficiently labeled with PET radionuclide ^{64}Cu at a specific activity of 222 MBq/nmol particles (or 4 $\mu\text{Ci}/\mu\text{g}$ Fe) with a radiolabeling yield of 60–70%. Figure 4a showed the representative coronal and transverse PET and computed tomography (CT) images of HT-29 tumor-bearing mice at 4 and 24 h after tail-vein injection of 100 μCi of ^{64}Cu -DB-HNTs. The HT-29 tumor was clearly visualized with high contrast relative to the background after 4 and 24 h post-injection of radiolabeled NPs. On the basis of the quantitative analysis of region of interest (ROI), PET images revealed that the tumor accumulation of radiolabeled NPs at 4 h post-injection was 2.7 ± 0.8 percentage injected dose per gram (%ID/g) and increased to 4.0 ± 1.0 %ID/g after 24 h post-injection. After accurate PET/CT image alignment, the nonspecific uptakes of NPs by major organs delineated and localized by CT images were detected and quantified in the PET images (Figure 4b). The liver and spleen uptake were prominent after 4 h post-injection (18.7 ± 1.1 , 11.5 ± 0.8 %ID/g), indicating a majority of injected NPs are taken up by the MPS. A significant decrease (5.1%ID/g) in liver uptake after 24 h post-injection highlighted that NPs were able to be eliminated through hepatic excretion. More importantly, the kidney uptake of injected NPs was 3.5 ± 0.5 %ID/g at 4 h post-injection and slightly increased to 4.1 ± 0.5 %ID/g after 24 h post-injection, indicating that the renal excretion was also involved in the elimination process of NPs from mice. Even though XDB-HNTs have slightly bigger sizes than DB-HNTs, they show very similar *in vivo* behavior as DB-HNTs (Figure 4c,d). The favorable *in vivo* distribution, tumor accumulation and clearance through both hepatobiliary and renal system indicate that the DB-HNTs is a novel type of highly promising NPs for *in vivo* applications.

Dual T_1 and T_2 -Weighted MRI. To validate the ability of Gd–DB-HNTs as dual T_1/T_2 mode MRI agents in living subjects, we performed the *in vivo* MRI of mice bearing HT-29 tumors injected *via* the tail vein with Gd–DB-HNTs (200 μL , 8 mg Fe/kg mouse body weight). When administered in the bloodstream, the Gd–DB-HNTs favor extravasations through leaky vasculature due to their size and surface properties, followed by deep penetration and retention at the tumor sites, which is a phenomenon known as the Enhanced

Permeability and Retention (EPR) effect. Figure 4e shows the transverse T_1 - and T_2 -weighted images of tumor before injection and at 4 h post-injection. Compared with the pre-injection images, T_1 -weighted tumor images showed obvious positive signal enhancement, while the tumor signal from T_2 -weighted images was getting much darker. Since the tumor appeared hyperintense relative to muscle on T_2 -weighted images before tail-vein injection of Gd–DB-HNTs, it consequently became easily identifiable on the post-injection images because of the obvious hypointensities within the tumors. Such a significant change in contrast was attributed to the accumulation of the injected Gd–DB-HNTs in the tumor *via* the EPR effect. On the other hand, the hyperintense signal from the tumor sites on T_1 -weighted image after intravenous injection of particles further validated that Gd–DB-HNTs were accumulated within the tumor after 4 h. As seen in Figure 4e, the variation in the signal intensities on T_1 -weighted and T_2 -weighted images most likely reflected the inhomogeneities of tumors, such as tumor vessel, cell density, necrotic core, or susceptibility effects between tissues. Although calculated T_1 or T_2 maps could clearly identify those substantial changes in T_1 or T_2 values in the ROIs compared to the surrounding tissues, the quantification of the concentration of accumulated Gd–DB-HNTs within the tumors from T_1 or T_2 measurement is inexact, possibly due to the lack of correlation between the number of the particles and either T_1 or T_2 value, especially when monitoring tumor uptake overtime.³⁰ To obtain the reproducible and dependable results for signal intensity measurement, we manually drew ROIs covering the whole tumor volume on both T_1 - and T_2 -weighted images. According to quantification analysis of the MR signal in the tumors, there was a sharp increase (36%) in T_1 -weighted signal intensity after 4 h post-injection, while the T_2 -weighted signal intensity was decreased to 72% of initial scans (Figure 4f). These results indicated that Gd–DB-HNTs provided both positive T_1 and negative T_2 contrast enhancement for MR tumor imaging. It is worth noting that, when the T_1 and T_2 contrast intensities are comparable, the dual-contrast effect probes could provide optimal contrasts on both T_1 - and T_2 -weighted images because of their synergistic combination of the two relaxation effects.

CONCLUSIONS

By fusing Au, Pt, and IONP nanocrystals together *via* solid-state interfaces, and selectively modifying distinct surfaces, we built hybrid nanotrimers to combine both T_1 and T_2 -weighted contrast agents together in a nano-composite with desirable shape and size for dual MRI. We further manipulated the spatial arrangement of each component in order to control the distance between T_1

and T_2 species to reduce the magnetic coupling and synergistically enhance both T_1/T_2 contrast effects. The novel nanostructures having both positive and negative

contrast effects can be potentially used as molecular nanoprobes for tumor diagnostic and therapeutic applications with excellent accuracy and reliability.

METHODS

Materials. Hydrogen tetrachloroaurate(III) (HAuCl_4) and platinum(II) 2,4-pentanedionate ($\text{Pt}(\text{acac})_2$) were ordered from Strem Chemicals, Inc. *N*-Hydroxysuccinimide (NHS), *N*-hydroxysulfosuccinimide (sulfo-NHS), and 1-ethyl-3-(3-(dimethylamino)propyl)carbodiimide hydrochloride (EDC) were purchased from Pierce Biotechnology. Iron pentacarbonyl [$\text{Fe}(\text{CO})_5$], oleic acid (technical grade 90%), oleylamine (technical grade 90%), 1-octadecene (technical grade 90%), cystamine, and methoxyPEG glycol (mPEG 5000) were ordered from Sigma/Aldrich. The metal chelator, 1,4,7,10-tetraazacyclododecane-1,4,7,10-tetraacetic acid mono (*N*-hydroxysuccinimide ester), DOTA-NHS-ester, was obtained from Macrocyclics. Unless otherwise mentioned, all other chemicals were purchased from Sigma/Aldrich. All solvents and chemicals were used as received. The radioisotope ^{64}Cu was provided by the Department of Medical Physics, University of Wisconsin at Madison (Madison, WI). Dotarem (Gd-DOTA) was purchased from Guerbet, Inc.

Characterizations. Mass spectra of synthetic polymers were recorded by a time-of-flight (TOF) mass spectrometer (AB SCIEX TOF/TOF 5800, Applied Biosystems) equipped with a matrix-assisted laser desorption ionization (MALDI) ion source. A CRC-15R PET dose calibrator (Capintec Inc., Ramsey, NJ) was used for all radioactivity measurements. Graphical image analysis was performed using ImageJ. The elemental analyses were performed using inductively coupled plasma mass spectrometer (ICP-MS, Thermo Scientific Xseries 2 Quadrupole). The NP samples were suspended in freshly prepared *aqua regia* [trace metal grade 70% nitric acid HNO_3 /36% hydrochloric acid HCl (Fisher Scientific), 1:3 v/v] and heated until completely dissolved, and then diluted up to 8 mL with double-distilled water. The cells pallets, homogenized tissues and organs (no more than 500 mg) were digested in a microwave (CEM MarsXpress Microwave Digester with Teflon microwave-safe vessels) before ICP analysis. The high-resolution transmission electron microscope (HR-TEM) and scanning transmission electron microscope (STEM) images were recorded with a FEI Tecnai G2 F20 X-TWIN transmission electron microscope operating at 200 kV. Samples were deposited and dried on copper grids covered with a Formvar/carbon support film, followed by plasma cleaning.

Synthesis of Au–IONPs. The dumbbell-like Au–IONP heterodimers (Au–IONP) were prepared using previously published procedure.²³

Synthesis of HNTs, Dumbbell HNTs (DB-HNTs), and Extra Large Dumbbell HNTs (XDB-HNTs). The 4, 5, and 7 nm cubic Pt NPs and Pt–IONP heterodimers (Pt–IONPs) were synthesized according to the procedures described in the previous publications.^{26–28} The HNTs and DB-HNTs were prepared using a modified procedure.²⁷ Experimentally, 20 mg of hydrogen tetrachloroaurate(III) (HAuCl_4) was dissolved in 10 mL of 1-octadecene containing 0.5 mL of oleylamine in a 20 mL glass vial with vigorous stirring. Under a nitrogen flow, Pt–IONPs (10 mg) in 1 mL of hexane were quickly injected into the above solution at 80 °C. The Au epitaxial overgrowth on Pt–IONPs was carried out at this temperature for 2 h to yield a purple-dark gray colloidal solution. After the mixture was cooled down to room temperature, the resultant DB-HNTs were precipitated by adding 40 mL of isopropyl alcohol and collected by centrifugation (5000 rpm, 5 min). When 5 nm cubic Pt NPs were used as seeds, the XDB-HNTs were obtained by the same procedure. The HNTs were obtained by a similar procedure when 10 mg of HAuCl_4 was used as a gold precursor. The precipitated NPs were redispersed in 5 mL of hexanes in the presence of 0.02 mL of oleylamine, and were recollected by ethanol precipitation and centrifugation. The washing process was repeated twice and the final products

were stored in hexanes (5 mL) in the presence of 0.02 mL of oleylamine.

Synthesis of Cystamine–DOTA₂. The cystamine dihydrochloride (1.5 mg, 6.5 μmol) was dissolved in 0.2 mL of DMF containing 5 μL of *N,N*-diisopropylethylamine. Ten milligrams of DOTA–NHS-ester in 50 μL of DMF was added to the above solution. The resultant mixture was stirred for 4 h at room temperature and the completion of the reaction was monitored by Kaiser test and mass spectra. The final product was identified by MALDI-TOF (Supporting Information Figure S9).

Synthesis of Methoxypolyethylene Glycol 5000 Acid (mPEG-5000-COOH). To a solution of methoxy polyethylene glycol 5000 (5 g, 1 mmol) in 30 mL of dry THF was slowly added sodium hydride (60%, 0.2 g, 5 mmol) at room temperature. The solution was stirred for 1 h at room temperature, and then ethyl bromoacetate (1.11 mL, 10 mmol) was added dropwise. The mixture was stirred at 50 °C for 24 h. The solution was filtered and concentrated in vacuum. The residue was hydrolyzed with 20 mL of 1 M NaOH/methanol (1:1, v/v) for 6 h at room temperature. The resultant solution was acidified with 1 M HCl to pH 1.0, and the solvents were then removed under reduced pressure. The residue was dissolved in 10 mL of DCM and dried out in the presence of anhydrous sodium sulfate. The crude product was precipitated by adding cold ethyl ether and purified by chromatography to afford product mPEG-5000-COOH as a white powder.

Surface Modification of Various HNTs. Two milligrams of EDAC and 1.5 mg of NHS were added to the solution of the mPEG-5000-COOH (50 mg) in 2 mL of chloroform. The mixture was stirred at room temperature for 30 min, and 2 mg of dopamine in 1 mL of DMF with 2 mg of anhydrous sodium carbonate was then added. The resultant mixture was continuously stirred for 2 h at room temperature. Ten milligrams of dumbbell HNTs (HNTs, DB-HNTs, or XDB-HNTs) in 1 mL of chloroform was added to the above mixture with vigorous stirring. The resulting mixture was stirred at room temperature for 24 h. The PEGylated nanoparticles were precipitated by adding 15 mL of hexane, and collected by centrifugation. After a wash with hexane, the PEGylated HNTs were redissolved in 2 mL of chloroform. Ten milligrams of as-synthesized cystamine–DOTA₂ in 1 mL of DMF was added to the solution. The resultant mixture was vigorously stirred for 24 h at room temperature. The modified HNTs were precipitated by adding 15 mL of hexane, and collected by centrifugation. The washing process was repeated twice. The NPs were dried under the nitrogen flow and redissolved in water. The NPs were purified by dialysis tubing (MWCO = 12 kDa). After a pass through 0.22 μm filter, the resultant NPs were concentrated using a spin filter (MWCO = 30 kDa). The concentrations of Au, Pt, and Fe were determined by ICP-MS analysis. The same procedure was used to modify Au–IONP and HNTs.

TEM Analysis. The TEM images were recorded with a FEI Tecnai G2 F20 X-TWIN transmission electron microscope operating at 200 kV. Samples were deposited and dried on copper grids covered with a Formvar/carbon support film, followed by plasma cleaning. The crystal sizes of each component of HNTs were measured using TEM. The characterization of sizes of NPs by TEM was performed according to the standard assay protocol (NIST - NCL Joint Assay Protocol, PCC-7), including sample preparation, measurement and result analysis. A minimum of 200 discrete particles was measured from each of at least two widely separated regions of the sample. Version V1.46 of NIH ImageJ was used for image processing, analysis and measurements.

Stability Test. The colloidal stability of DB-HNTs in aqueous solution was studied by dynamic light scattering (Malvern Zeta Size Nano S-90 DLS instrument). The refractive indexes of gold

and platinum were adapted from the Malvern Reference manual (MAN0396 Issue 1.0). The refractive index of 0.30 was adapted for gold, while the refractive index of platinum was 4.5. The stability of functionalized DB-HNTs was validated by measuring the hydrodynamic size distribution of functionalized DB-HNTs in serum using DLS. The DB-HNTs were added to mouse serum in phosphate buffered saline (PBS) at a concentration of 4 nM and then incubated at 37 °C for 24 h. The aliquots were analyzed at 0, 4, 8, 24, and 48 h post-incubation by DLS. Each aliquot was filtered using a spin filter (MWCO = 30 kDa), and further washed with water 3 times. The eluent was collected and analyzed by ICP-MS for trace amount of Fe, Pt, Au and Gd.

Cytotoxicity Assay. Cytotoxicity of Gd–DB-HNTs was evaluated by using a cell viability assay (MTT, (3-(4,5-dimethylthiazol-2-yl)-2,5-diphenyl tetrazolium bromide (Sigma-Aldrich, St. Louis, MO))). Briefly, NIH-3T3 cells were plated into a 96-well plate at a concentration of 6×10^3 cells/well in DMEM with 10% fetal bovine serum (FBS) at 37 °C and 5% CO₂, and 24 h later, the cells were incubated with Gd–DB-HNTs with different concentrations in DMEM for 24 and 48 h. The cell viability assays were carried out according to the manufacturer's instruction. After treatment, MTT compound (5 mg/mL in PBS) was diluted 1:100 with DMEM medium into each well. After 3 h incubation, culture supernatants were carefully removed, and the purple reduced MTT product was redissolved in 100 μL of DMSO in 10 min. The concentration of the reduced MTT in each well was determined spectrophotometrically at 540 nm with a reference wavelength of 650 nm using a microplate reader (TECAN Infinite M100). All samples were done in triplicate and all experiments were repeated 3–5 times. MTT absorbance values were normalized to 100%; experimental values (treated) were expressed as percentage of the control. Significant differences between sets of values for control and test groups were assessed by Student's *t* test.

Gd Chelating of DOTA-Modified DB-HNTs or XDB-HNTs. The gadolinium chloride solution (100 μL of 10 mM in 0.1 M sodium acetate buffer (pH = 6)) was added to 0.5 mL of 150 nM DOTA DB-HNTs solution with 100 μL of 0.1 M sodium acetate buffer in a microcentrifuge tube. The tube was incubated at a 42 °C water bath overnight for the chelating reaction. The unbound Gd ions were removed by using a PD-10 column. The eluent was concentrated using a spin filter (MWCO = 30 kDa), and further washed with water 3 times. The concentrations of Au, Pt, Gd, and Fe were determined by ICP–MS analysis.

Relaxivity Measurement. A series of concentrations of four types of Gd-incorporated NPs (0, 0.0156, 0.0312, 0.0625, 0.125, 0.25, 0.5, and 1 mM Fe; the corresponding Gd concentrations are determined by the molar ratios of Fe to Gd based on Table 1) were prepared by dilution in 1% agarose gel and then were solidified in the 300 μL vials. The longitudinal (r_1) and transverse relaxation rates (r_2) of various heterostructures (Gd–HNTs, Gd–DB-HNTs, or Gd–XDB-HNTs) were measured using a 7.0-T small animal MRI system with magnetic bore size of 310 mm, including a superconducting magnet (Magnex Scientific) with 7.0 T field strength and a gradient with 120 mm i.d., 600 mT/m of maximum gradient amplitude, and 6000 T/m/s of a maximum slew rate. T_1 -weighted MR images were acquired using fast-spin echo sequences under the following parameters: echo time (T_E)/repetition time (T_R) = 10/750 ms, 256 × 256 matrix, 1 NEX, 8 cm field of view (FOV), and slice thickness of 1 mm. The in-plane resolution is 313 × 313 μm². T_1 mapping images were acquired using an inversion recovery sequence (T_E/T_R = 10/6000 ms) with inversion time (T_I) of 50, 100, 200, 500, 750, 1000, 1250, 1500, 2000, 2500, and 3000 ms. On each image, signal intensities were measured by drawing ROIs in the center of each vial. The T_1 relaxation times were performed by fitting the acquired inversion recovery images to a following equation: $M = M_0(1 - 2 \exp(-T_I/T_1) + \exp(-T_R/T_1))$, where M and M_0 are measured and initial magnetization, respectively. T_2 -weighted MR images were obtained using fast-spin echo sequences under the following parameters: T_E/T_R = 40/4000 ms, 256 × 256 matrix, 1 NEX, 8 cm field of view with an in-plane resolution of 313 × 313 μm², and slice thickness of 1 mm. T_2 maps were obtained using a spin-echo sequence with the following parameters: T_E = 10, 20, 40, 60, 80, 100, 120, and 140 ms, T_R = 4000 ms,

FOV = 8 cm, 256 × 256 matrix, 1 NEX, and slice thickness of 1 mm. The T_2 quantification was performed by curve-fitting the analytical equation: $M = M_0 \exp(-T_E/T_2)$. All data fittings were performed using a nonlinear least-squares algorithm implemented in the OriginPro 8.1 SR2 (OriginLab Co.) analysis software.

⁶⁴Cu Radiolabeling of DOTA-Modified DB-HNTs or XDB-HNTs and Serum

Stability Study. The ⁶⁴Cu radiolabeling procedure was conducted according to a slightly modified procedure published previously.²³ Typically, the ⁶⁴Cu stock solution (CuCl₂) was diluted with 200 μL of 100 mM sodium acetate buffer (pH = 5.0) before making the final pH adjustment using 0.1 M NaOH solution. Twenty microliters of ⁶⁴Cu stock solution (1 mCi, 37 MBq) was then added to 200 μL of 100 nM DOTA-DB-HNTs or DOTA-XDB-HNTs with 150 μL of 0.1 M sodium acetate buffer. The mixture was then incubated at 40 °C for 1 h, and the radiolabeled NPs were applied to a size-exclusion column (PD-10) and eluted with PBS. The eluents were collected and the resultant ⁶⁴Cu-DB-HNTs or ⁶⁴Cu-XDB-HNTs have modest specific activity (222 MBq/nmol particle, 4 μCi/μg Fe). The serum stability of ⁶⁴Cu labeled NPs was performed according to our previous report.²³ Briefly, ⁶⁴Cu-DB-HNTs or ⁶⁴Cu-XDB-HNTs were incubated in mouse serum at 37 °C for up to 24 h. Aliquots of the mixture were removed from the solution at predetermined time intervals and filtered through 30 kDa cutoff filters. The radioactivity of filtrates was then measured. The stability of radiolabels NPs was calculated by the percentages of retained ⁶⁴Cu on the NPs to the total activity. Samples were assayed in triplicate.

Cell Culture and Tumor Xenograft Model. The HT-29 (human colorectal adenocarcinoma cell line) cells were purchased from the American Type Culture Collection (ATCC, Manassas, VA). The HT-29 cells were cultured in McCoy's 5a medium [10% heat-inactivated FBS and 1% penicillin–streptomycin] and propagated as recommended by ATCC. Female *nu/nu* mice (Charles River Laboratories International, Inc., Wilmington, MA) were housed and maintained in accordance with federal and local institutional rules for the conduct of animal experimentation and received food and water *ad libitum*. Tumors were generated by harvesting HT-29 cells from mid-log phase cultures using Trypsin–EDTA (Invitrogen, Inc.). Approximately 4×10^6 HT-29 cells suspended in 100 μL of PBS were subcutaneously implanted in the right shoulders of nude mice. Tumors were allowed to grow to a size of 600–800 mm³ (3–4 weeks) before imaging experiments.

In Vivo Small-Animal PET/CT of Tumor Mice. ⁶⁴Cu-DOTA-HNTs or ⁶⁴Cu-DOTA-HNTs (100 μCi in 150 μL PBS) were injected *via* tail vein into the HT-29 tumor-bearing mice (*n* = 3) at a dose of 5 mg Fe/kg of mouse weight. *In vivo* small-animal PET/CT was carried out on a Siemens-Inveon PET-CT (Siemens Medical Solution) according to the previous publications.^{31,32} PET scans were performed at 4 and 24 h post-injection (pi). Mice were anesthetized with isoflurane (5% for induction and 2% for maintenance in 100% O₂). With the help of a laser beam attached to the scanner, mice were placed in the prone position and near the center of the field of view (FOV) of the scanner and 5 min static scans were obtained. All the small animal PET images were reconstructed and viewed by the *Inveon* Research Workplace (IRW). Region of interests (ROIs for coronal and transaxial slices) were drawn over the tumor on decay-corrected whole-body coronal images. Values in 3 to 10 adjacent slices (depending on the size of the tissue or organ) were averaged to obtain a reproducible value of radioactivity concentration. The maximum counts per pixel per minute were obtained from the ROIs and were converted to counts per milliliter per minute using a calibration constant. ROIs were then converted to counts per gram per minute based on the assumption of a tissue density of 1 g/mL, and image ROI-derived percentage of the injected radioactive dose per gram of tissue (%ID/g) values were determined by dividing counts per gram per minute by injected dose. No attenuation correction was performed.

MRI. Mice bearing HT-29 tumor were anesthetized with 2% isoflurane in oxygen and placed with prone position. MRI was performed using the same instrument, protocols, and conditions as in the phantom MRI study. DOTA-DB-HNTs were injected *via* tail vein into the HT-29 tumor-bearing mice at a

dose of 10 mg Fe/kg of mouse weight ($n = 3$). T_2 -weighted fast spin-echo MR images were acquired on a 7.0-T small animal MRI system (GE Healthcare) under the following parameters: repetition time (T_R) = 3000 ms, T_E = 40 ms, echo train length = 8, FOV = 4 × 4 cm², section thickness = 1 mm, flip angle = 90°. MR images were acquired in both transverse and coronal direction pre-injection and at 4 and 48 h after injection. Transversal and coronal MR images were acquired and the signal intensities were measured in defined ROIs using OsiriX imaging software (OsiriX version 3.2; Apple Computer). The NIH standard was used for tumor imaging processing. The ROI analysis was performed according to the previous publications.²³

Statistical Method. Measurement data are expressed as the mean ± SD. Statistical analyses of the data were performed using Prism (GraphPad Software). A *p*-value of less than 0.05 was considered significant.

Conflict of Interest: The authors declare no competing financial interest.

Acknowledgment. This work was supported, in part, by the Office of Science (BER), U.S. Department of Energy (DE-SC0008397) and NCI of Cancer Nanotechnology Excellence Grant CCNE-TR U54 CA119367.

Supporting Information Available: TEM images of Pt–IONPs, HRTEM images of HNTs, mass spectra of mPEG-5000-COOH, hydrodynamic sizes of functional Au–IONPs, HNTs, and DB-HNTs and XDB-HNTs, zeta potentials of Gd incorporated DB-HNTs, and stability test of Gd–DB-NHTs. This material is available free of charge via the Internet at <http://pubs.acs.org>.

REFERENCES AND NOTES

1. Frey, N. A.; Peng, S.; Cheng, K.; Sun, S. Magnetic Nanoparticles: Synthesis, Functionalization, and Applications in Bioimaging and Magnetic Energy Storage. *Chem. Soc. Rev.* **2009**, *38*, 2532–2542.
2. Caravan, P. Protein-Targeted Gadolinium-Based Magnetic Resonance Imaging (MRI) Contrast Agents: Design and Mechanism of Action. *Acc. Chem. Res.* **2009**, *42*, 851–862.
3. Qin, C.; Cheng, K.; Chen, K.; Hu, X.; Liu, Y.; Lan, X.; Zhang, Y.; Liu, H.; Xu, Y.; Bu, L.; Su, X.; Zhu, X.; Meng, S.; Cheng, Z. Tyrosinase as a Multifunctional Reporter Gene for Photo-acoustic/MRI/PET Triple Modality Molecular Imaging. *Sci. Rep.* **2013**, *3* (1038), 1–8.
4. Na, H. B.; Song, I. C.; Hyeon, T. Inorganic Nanoparticles for MRI Contrast Agents. *Adv. Mater.* **2009**, *21*, 2133–2148.
5. Lee, S. H.; Kim, B. H.; Na, H. B.; Hyeon, T. Paramagnetic Inorganic Nanoparticles as T1MRI Contrast Agents. *Wiley Interdiscip. Rev.: Nanomed. Nanobiotechnol.* **2014**, *6*, 196–209.
6. Steinbacher, J. L.; Lathrop, S. A.; Cheng, K.; Hillegass, J. M.; Butnor, K. J.; Kauppinen, R. A.; Mossman, B. T.; Landry, C. C. Gd-Labeled Microparticles in MRI: *In Vivo* Imaging of Microparticles after Intraperitoneal Injection. *Small* **2010**, *6*, 2678–2682.
7. Courant, T.; Roullin, V. G.; Cadiou, C.; Callewaert, M.; Andry, M. C.; Portefaix, C.; Hoeffel, C.; de Goltstein, M. C.; Port, M.; Laurent, S.; Elst, L. V.; Muller, R.; Molinari, M.; Chuburu, F. Hydrogels Incorporating GdDOTA: Towards Highly Efficient Dual T1/T2MRI Contrast Agents. *Angew. Chem., Int. Ed.* **2012**, *51*, 9119–9122.
8. Jun, Y. W.; Lee, J. H.; Cheon, J. Chemical Design of Nanoparticle Probes for High-Performance Magnetic Resonance Imaging. *Angew. Chem., Int. Ed.* **2008**, *47*, 5122–5135.
9. Laurent, S.; Forge, D.; Port, M.; Roch, A.; Robic, C.; Vander Elst, L.; Muller, R. N. Magnetic Iron Oxide Nanoparticles: Synthesis, Stabilization, Vectorization, Physicochemical Characterizations, and Biological Applications. *Chem. Rev.* **2008**, *108*, 2064–2110.
10. Choi, J.-s.; Lee, J.-H.; Shin, T.-H.; Song, H.-T.; Kim, E. Y.; Cheon, J. Self-Confirming “AND” Logic Nanoparticles for Fault-Free MRI. *J. Am. Chem. Soc.* **2010**, *132*, 11015–11017.
11. Kim, B. H.; Lee, N.; Kim, H.; An, K.; Park, Y. I.; Choi, Y.; Shin, K.; Lee, Y.; Kwon, S. G.; Na, H. B.; Park, J.-G.; Ahn, T.-Y.; Kim, Y.-W.; Moon, W. K.; Choi, S. H.; Hyeon, T. Large-Scale Synthesis of Uniform and Extremely Small-Sized Iron Oxide Nanoparticles for High-Resolution T1Magnetic Resonance Imaging Contrast Agents. *J. Am. Chem. Soc.* **2011**, *133*, 12624–12631.
12. Seo, W. S.; Lee, J. H.; Sun, X.; Suzuki, Y.; Mann, D.; Liu, Z.; Terashima, M.; Yang, P. C.; McConnell, M. V.; Nishimura, D. G.; Dai, H. FeCo/Graphitic-Shell Nanocrystals as Advanced Magnetic-Resonance-Imaging and Near-Infrared Agents. *Nat. Mater.* **2006**, *5*, 971–976.
13. Xiao, J.; Tian, X. M.; Yang, C.; Liu, P.; Luo, N. Q.; Liang, Y.; Li, H. B.; Chen, D. H.; Wang, C. X.; Li, L.; Yang, G. W. Ultrahigh Relaxivity and Safe Probes of Manganese Oxide Nanoparticles for *in Vivo* Imaging. *Sci. Rep.* **2013**, *3* (3324), 1–7.
14. Xu, W.; Kattel, K.; Park, J. Y.; Chang, Y.; Kim, T. J.; Lee, G. H. Paramagnetic Nanoparticle T1 and T2MRI Contrast Agents. *Phys. Chem. Chem. Phys.* **2012**, *14*, 12687–12700.
15. Na, H. B.; Song, I. C.; Hyeon, T. Inorganic Nanoparticles for MRI Contrast Agents. *Adv. Mater.* **2009**, *21*, 2133–2148.
16. Hu, F.; Zhao, Y. S. Inorganic Nanoparticle-based T1 and T1/T2Magnetic Resonance Contrast Probes. *Nanoscale* **2012**, *4*, 6235–6243.
17. Na, H. B.; Lee, J. H.; An, K.; Park, Y. I.; Park, M.; Lee, I. S.; Nam, D. H.; Kim, S. T.; Kim, S. H.; Kim, S. W.; Lim, K. H.; Kim, K. S.; Kim, S. O.; Hyeon, T. Development of a T1 Contrast Agent for Magnetic Resonance Imaging Using MnO Nanoparticles. *Angew. Chem. Int. Ed.* **2007**, *46*, 5397–5401.
18. Kim, T.; Momin, E.; Choi, J.; Yuan, K.; Zaidi, H.; Kim, J.; Park, M.; Lee, N.; McMahon, M. T.; Quinones-Hinojosa, A.; Bulte, J. W.; Hyeon, T.; Gilad, A. A. Mesoporous Silica-coated Hollow Manganese Oxide Nanoparticles as Positive T1 Contrast Agents for Labeling and MRI Tracking of Adipose-derived Mesenchymal Stem Cells. *J. Am. Chem. Soc.* **2011**, *133*, 2955–2961.
19. Na, H. B.; Hyeon, T. Nanostructured T1MRI Contrast Agents. *J. Mater. Chem.* **2009**, *19*, 6267–6273.
20. Bae, K. H.; Kim, Y. B.; Lee, Y.; Hwang, J.; Park, H.; Park, T. G. Bioinspired Synthesis and Characterization of Gadolinium-Labeled Magnetite Nanoparticles for Dual Contrast T1- and T2-Weighted Magnetic Resonance Imaging. *Bioconjugate Chem.* **2010**, *21*, 505–512.
21. Yang, H.; Zhuang, Y.; Sun, Y.; Dai, A.; Shi, X.; Wu, D.; Li, F.; Hu, H.; Yang, S. Targeted Dual-contrast T1- and T2-Weighted Magnetic Resonance Imaging of Tumors Using Multifunctional Gadolinium-Labeled Superparamagnetic Iron Oxide Nanoparticles. *Biomaterials* **2011**, *32*, 4584–4593.
22. Zhou, Z.; Huang, D.; Bao, J.; Chen, Q.; Liu, G.; Chen, Z.; Chen, X.; Gao, J. A Synergistically Enhanced T1–T2 Dual-Modal Contrast Agent. *Adv. Mater.* **2012**, *24*, 6223–6228.
23. Yang, M.; Cheng, K.; Qi, S. B.; Liu, H. G.; Jiang, Y. X.; Jiang, H.; Li, J. B.; Chen, K.; Zhang, H. M.; Cheng, Z. Affibody Modified and Radiolabeled Gold-Iron Oxide Hetero-Nanostructures for Tumor PET, Optical and MR Imaging. *Biomaterials* **2013**, *34*, 2796–2806.
24. Yu, H.; Chen, M.; Rice, P. M.; Wang, S. X.; White, R. L.; Sun, S. Dumbbell-like Bifunctional Au-Fe₃O₄ Nanoparticles. *Nano Lett.* **2005**, *5*, 379–382.
25. Xu, C.; Xie, J.; Ho, D.; Wang, C.; Kohler, N.; Walsh, E. G.; Morgan, J. R.; Chin, Y. E.; Sun, S. Au-Fe₃O₄ Dumbbell Nanoparticles as Dual-functional Probes. *Angew. Chem., Int. Ed.* **2008**, *47*, 173–176.
26. Wang, C.; Daimon, H.; Onodera, T.; Koda, T.; Sun, S. A General Approach to the Size- and Shape-Controlled Synthesis of Platinum Nanoparticles and Their Catalytic Reduction of Oxygen. *Angew. Chem., Int. Ed.* **2008**, *47*, 3588–3591.
27. Buck, M. R.; Bondi, J. F.; Schaak, R. E. A Total-Synthesis Framework for the Construction of High-Order Colloidal Hybrid Nanoparticles. *Nat. Chem.* **2012**, *4*, 37–44.
28. Cheng, K.; Kothapalli, S.-R.; Liu, H.; Koh, A. L.; Jokerst, J. V.; Jiang, H.; Yang, M.; Li, J.; Levi, J.; Wu, J. C.; Gambhir, S. S.; Cheng, Z. Construction and Validation of Nano Gold Tripods for Molecular Imaging of Living Subjects. *J. Am. Chem. Soc.* **2014**, *136*, 3560–3571.
29. Wang, C.; Wei, Y.; Jiang, H.; Sun, S. Tug-of-War in Nanoparticles: Competitive Growth of Au on Au–Fe₃O₄ Nanoparticles. *Nano Lett.* **2009**, *9*, 4544–4547.

30. Thu, M. S.; Bryant, L. H.; Coppola, T.; Jordan, E. K.; Budde, M. D.; Lewis, B. K.; Chaudhry, A.; Ren, J.; Varma, N. R. S.; Arbab, A. S.; Frank, J. A. Self-assembling Nanocomplexes by Combining Ferumoxytol, Heparin and Protamine for Cell Tracking by Magnetic Resonance Imaging. *Nat. Med.* **2012**, *18*, 463–467.
31. Miao, Z.; Ren, G.; Liu, H.; Jiang, L.; Cheng, Z. Cy5.5-Labeled Affibody Molecule for Near-infrared Fluorescent Optical Imaging of Epidermal Growth Factor Receptor Positive Tumors. *J. Biomed. Opt.* **2010**, *15*, 036007-1–036007-7.
32. Miao, Z.; Ren, G.; Liu, H.; Jiang, L.; Cheng, Z. Small-animal PET Imaging of Human Epidermal Growth Factor Receptor Positive Tumor with a ⁶⁴Cu Labeled Affibody Protein. *Bioconjugate Chem.* **2010**, *21*, 947–954.